6.2 Commensurable periodic structures

In the preceding section, we discussed the spin-wave spectra in helical or conical systems, which are characterized by the important feature that the magnitude of the ordered moments, and hence of the exchange field, are constant. This simplification allowed an analytic derivation of the spin-wave energies, in weakly anisotropic systems. If B_6^6 only leads to a slight distortion of the structure, its effects on the spin waves may be included as a perturbation. If B_6^6 is large, however, as it is for instance in Ho, this procedure may not be sufficiently accurate. Instead it is necessary to diagonalize the MF Hamiltonian for the different sites, determine the corresponding MF susceptibilities, and thereafter solve the site-dependent RPA equation

$$\overline{\overline{\chi}}(ij,\omega) = \overline{\overline{\chi}}_i^{\,o}(\omega)\delta_{ij} + \sum_{j'} \overline{\overline{\chi}}_i^{\,o}(\omega)\overline{\overline{\mathcal{J}}}(ij')\overline{\overline{\chi}}(j'j,\omega). \tag{6.2.1}$$

In uniform para- or ferromagnetic systems, $\overline{\overline{\chi}}_i^{\,o}(\omega)$ is independent of the site considered, and the equation may be diagonalized, with respect to the site dependence, by a Fourier transformation. In an undistorted helix or cone, the transformation to the rotating coordinate system eliminates the variation of $\overline{\overline{\chi}}_i^{\,o}(\omega)$ with respect to the site index, and (6.2.1) may be solved as in the uniform case. If B_6^6 is large, the transformation to a (uniformly) rotating coordinate system leaves a residual variation in $\overline{\overline{\chi}}_i^{\,o}(\omega)$, and in the direction of the moments relative to the z-axis of the rotating coordinates. This complex situation can usually only be analysed by numerical methods. A strong hexagonal anisotropy will normally cause the magnetic structure to be commensurable with the lattice, as discussed in Section 2.3. We shall assume this condition, and denote the number of ferromagnetic hexagonal layers in one commensurable period by m, with $\mathbf{Q}$ along the c-axis. The spatial Fourier transformation of (6.2.1) then leaves m coupled equations. In order to write down these equations explicitly, we define the Fourier transforms

$$\overline{\overline{\chi}}^{\,o}(n;\omega) = \frac{1}{N}\sum_i \overline{\overline{\chi}}_i^{\,o}(\omega)\, e^{-in\mathbf{Q}\cdot\mathbf{R}_i} \tag{6.2.2a}$$

and, corresponding to (6.1.28),

$$\overline{\overline{\chi}}(n;\mathbf{q},\omega) = \frac{1}{N}\sum_{ij} \overline{\overline{\chi}}(ij,\omega)\, e^{-i\mathbf{q}\cdot(\mathbf{R}_i-\mathbf{R}_j)}\, e^{-in\mathbf{Q}\cdot\mathbf{R}_i}, \tag{6.2.2b}$$

where n is an integer. Equation (6.2.1) then leads to

$$\overline{\overline{\chi}}(n;\mathbf{q},\omega) = \overline{\overline{\chi}}^{\,o}(n;\omega) + \sum_{s=0}^{m-1} \overline{\overline{\chi}}^{\,o}(n-s;\omega)\overline{\overline{\mathcal{J}}}(\mathbf{q}+s\mathbf{Q})\overline{\overline{\chi}}(s;\mathbf{q},\omega), \tag{6.2.3}$$

where $\overline{\overline{\chi}}^o(n+m;\omega) = \overline{\overline{\chi}}^o(n;\omega)$. The m matrix equations may be solved by replacing ω by $\omega + i\epsilon$. Instead of taking the limit $\epsilon \to 0^+$, as required by the definition of the response function, ϵ is considered as non-zero but small, corresponding to a Lorentzian broadening of the excitations. Equation (6.2.3) may then be solved by a simple iterative procedure, after the diagonal term $\overline{\overline{\chi}}(n;\mathbf{q},\omega)$ has been isolated on the left-hand side of the equation. If m is not too large, and if ϵ is not chosen to be too small, this procedure is found to converge rapidly, requiring only 10–20 iterations at each $(\mathbf{q},\omega)$. The energies of the magnetic excitations at the wave-vector $\mathbf{q}$ are then derived from the position of the peaks, of width $2\hbar\epsilon$, in the calculated response function $\mathrm{Im}\big[\overline{\overline{\chi}}(0;\mathbf{q},\omega)\big]$.

The use of numerical methods, which is unavoidable in systems with complex moment-configurations, leads to less transparent results than those obtained analytically. However, compared with the linear spin-wave theory, they have the advantage that anisotropy effects may be included, even when they are large, without difficulty. The introduction of a non-zero value for ϵ means that the response function is only determined with a finite resolution, but this is not a serious drawback. The experimental results are themselves subject to a finite resolution, because of instrumental effects. Moreover, intrinsic linewidth phenomena, neglected within the RPA, provide a justification for adopting a non-zero ϵ.

The numerical method summarized above has been used for calculating the spin-wave energies in the various structures of Ho discussed in Section 2.3. In Fig. 5.9, we presented the dispersion relations in the c-direction of Ho containing 10% of Tb, in its ferromagnetic and helical phases (Larsen *et al.* 1987). The Tb content has the desirable effects of confining the moments to the basal plane, and inducing the simple bunched helix or zero-spin-slip structure (1.5.3) in the range 20–30 K, and ferromagnetism below 20 K. The commensurability of the 12-layer structure implies that the energy of the helix is no longer invariant under a uniform rotation, and an energy gap appears at long wavelengths, reflecting the force necessary to change the angle ϕ which the bunched moments make with the nearest easy axis. The excitations in this relatively straightforward structure can be treated by spin-wave theory, and the energies in the c-direction may be written in the form of eqn (6.1.10b):

$$E_\mathbf{q} = \big[A_\mathbf{q}^2 - B_\mathbf{q}^2\big]^{1/2},$$

where now

$$A_\mathbf{q} + B_\mathbf{q} = A + B + J\big\{\mathcal{J}_\parallel(\mathbf{0}) - \mathcal{J}_\parallel(\mathbf{q})\big\}, \qquad (6.2.4a)$$

and

$$A_\mathbf{q} - B_\mathbf{q} = A - B + u^2 J \{ \mathcal{J}_\perp(\mathbf{Q}) - \tfrac{1}{2} \mathcal{J}_\perp(\mathbf{q} + \mathbf{Q}) - \tfrac{1}{2} \mathcal{J}_\perp(\mathbf{q} - \mathbf{Q}) \}$$
$$+ v^2 J \{ \mathcal{J}_\perp(5\mathbf{Q}) - \tfrac{1}{2} \mathcal{J}_\perp(\mathbf{q} + 5\mathbf{Q}) - \tfrac{1}{2} \mathcal{J}_\perp(\mathbf{q} - 5\mathbf{Q}) \}. \quad (6.2.4b)$$

In this case, the axial- and hexagonal-anisotropy terms are

$$A + B = \frac{1}{J} \{ 6 B_2^0 J^{(2)} - 60 B_4^0 J^{(4)} + 210 B_6^0 J^{(6)} + 6 B_6^6 J^{(6)} \cos 6\phi \}$$
$$+ J \{ u^2 \mathcal{J}_\perp(\mathbf{Q}) + v^2 \mathcal{J}_\perp(5\mathbf{Q}) - \mathcal{J}_\parallel(\mathbf{0}) \}, \quad (6.2.5a)$$

and

$$A - B = 36 B_6^6 J^{(6)} \cos 6\phi, \quad (6.2.5b)$$

while u and v are determined from the bunching angle, by (1.5.3b), as respectively $\cos(\pi/12 - \phi)$ and $\sin(\pi/12 - \phi)$. As may be seen from the above expressions, the energy gap $E_\mathbf{0}$ in the periodic structure should be smaller than that in the ferromagnet by a factor of approximately $\cos 6\phi$, or about 0.8. The observed difference in Fig. 5.9 is considerably greater than this, and corresponds to an effective reduction of B_2^0 by about 50% in the helical phase. Such an effect can be accounted for by an anisotropic two-ion coupling of the type observed in Tb and considered in Section 5.5.2. Specifically, the term $\mathcal{C}(\mathbf{q})$ in eqn (5.5.19a) gives a contribution $\mathcal{C}(\mathbf{0})$ to $A + B$ in the ferromagnetic phase, and $\mathcal{C}(3\mathbf{Q}) \cos 6\phi$ in the bunched helical structure.

As in the ferromagnetic phase, treated in Section 5.5.1, the discontinuity in the dispersion relations at $\mathbf{q} = \mathbf{0}$ is due to the classical magnetic dipole–dipole interaction. As illustrated in Fig. 5.7, the basal-plane coupling $\mathcal{J}_\perp(\mathbf{q})$ has its maximum at $\mathbf{q} \simeq \mathbf{Q}$, but the jump in the long-wavelength limit in the dipolar contribution to $\mathcal{J}_\parallel(\mathbf{q}) - \mathcal{J}_\parallel(\mathbf{0})$, which has a magnitude $4\pi g \mu_B M$ or 0.28 meV, is sufficiently large that the absolute maximum in $\mathcal{J}_\parallel(\mathbf{q})$ is shifted from $\mathbf{q} = \mathbf{Q}$ to $\mathbf{q} = \mathbf{0}$. Consequently, the soft mode, whose energy goes to zero with the vanishing of the axial anisotropy at a temperature of 20 K in pure Ho, is the long-wavelength spin wave propagating perpendicular to the c-axis, rather than the mode of wave-vector $\mathbf{Q}$ along the c-axis. As discussed in Section 2.3.1, the cone structure, rather than the tilted helix, is thereby stabilized. Near the second-order phase transition, the divergence of $\chi_{\zeta\zeta}(\mathbf{0}, 0)$ is accompanied by a vanishing of the energy gap as $(T - T_C)^{1/2}$.

The calculated small energy gap at the centre of the zone in the commensurable helix, shown in Fig. 5.9, is due to the bunching of the moments; $\varphi = \pi/2 + p\pi/3 \pm \phi$, where the sign before ϕ alternates from
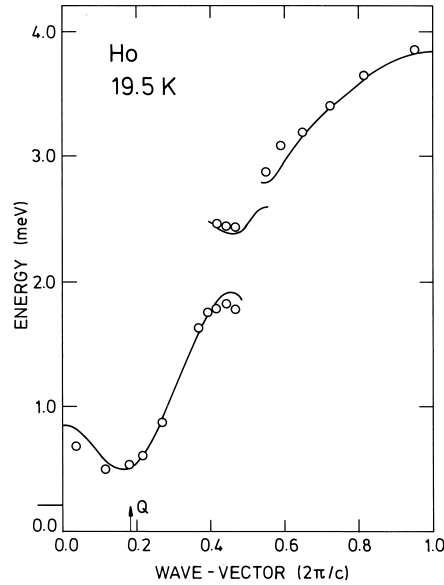
Fig. 6.4.   Magnetic excitations propagating in the c-direction in the one-spin-slip structure of Ho at $20\,\mathrm{K}$, after Patterson *et al.* (1990; and to be published). The full curve is the calculated dispersion relation and the points are the experimental results. The energy gap at $q = \frac{5}{11}(2\pi/c)$, due to the eleven-layer period, is resolved in these measurements. The linewidth of the scattering peaks behaves anomalously around $q = \frac{6}{11}(2\pi/c)$ suggesting a gap of the order of $0.3\,\mathrm{meV}$ at this wave-vector. The calculated energy of the long-wavelength modes in the basal plane is indicated by the line on the left. The discontinuity at $\mathbf{q} = \mathbf{0}$ is due to the dipolar coupling, and the transition to the cone structure is accompanied by a softening of this lowest-energy mode.

one layer to the next. This alternation doubles the periodicity in the rotating coordinate system, and thereby halves the Brillouin zone in the c-direction. The predicted gap is somewhat smaller than the experimental energy-resolution, and is therefore not observed in these measurements. The equivalent gap has however been measured in the one-spin-slip structure of Fig. 2.5 by Patterson *et al.* (1990), whose results are shown in Fig. 6.4. In this case, the 11-layer structure causes an eleven-fold reduction in the Brillouin zone, but only the first-order gap at $5/11$ times $2\pi/c$ is calculated to be readily observable. This gap, on the other hand, is amplified by about a factor two, as compared to that in the structure without spin slips. As the number of spin slips increases, the calculated excitation spectra (Jensen 1988a) become more complex,
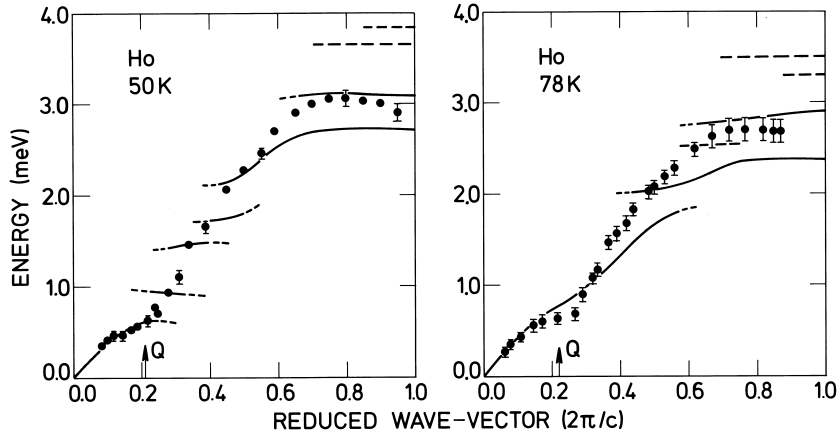
Fig. 6.5.   The energies of the magnetic excitations propagating in the *c*-direction in the 19-layer and 9-layer spin-slip structures of Fig. 2.5. The solid lines indicate the positions of the main peaks in the calculated spectrum, whereas the dashed extensions designate peaks of relatively lower intensities. The energy gaps due to the reduced symmetry are not resolved in the experimental measurements of Nicklow (1971).

as illustrated in Fig. 6.5. The dispersion relations are broken into short segments by a succession of energy gaps, which may however be difficult to identify because of intrinsic broadening effects, neglecting in the RPA, which become more and more pronounced at increasing temperatures.

At temperatures above about 50 K, when $\langle O_6^6 \rangle$ in Ho is small and the distortion of the helix correspondingly weak, the large B_6^6 still plays an important role in mixing $|J_z>$ molecular-field (MF) states. Indeed, as the temperature is increased and the exchange field decreases, this effect becomes relatively more important, so that, for example, the energy difference between the two lowest MF levels varies by an order of magnitude as the moment on the site moves from an easy to a hard direction at elevated temperatures, while this variation is much smaller in the low-temperature limit. The large changes in the MF states from site to site tend to disrupt the coherent propagation of the collective modes, providing a mechanism for the creation of energy gaps in the excitation spectrum. The spectrum thus becomes similar to that of the incommensurable longitudinal phase, illustrated in Fig. 6.3.

Whenever the moments are not along a direction of high symmetry, B_6^6 mixes the transverse and longitudinal components of the single-site susceptibility, so that the normal modes are no longer either pure transverse spin waves or longitudinal excitations. At low temperatures, where

$\langle J_z \rangle$ is close to its maximum value, this mixing is unimportant, but it has significant effects on the excitations at higher temperatures. In the RPA, the pure longitudinal response contains an elastic component, and the (mixed) excitation spectrum in the long-wavelength limit therefore comprises an elastic and an inelastic branch. The inelastic mode is calculated to lie around 1 meV in the temperature interval 50–80 K. In the RPA, this feature is independent of whether the magnetic periodicity is commensurable with the lattice. In the incommensurable structure, the free energy is invariant to a rotation of the helix around the c-axis, implying that $\overline{\overline{\chi}}_t(\mathbf{q}, \omega)$ diverges in the limit $(\mathbf{q}, \omega) \rightarrow (\mathbf{0}, 0)$. However, the corresponding generator of rotations no longer commutes with the Hamiltonian, as in the regular helix, because B_6^6 is now non-zero. The divergence of $\overline{\overline{\chi}}_t(\mathbf{q}, \omega)$ is therefore not reflected in a conventional Goldstone mode, but is rather manifested in the elastic, zero-energy phason mode, which coexists with the inelastic mode. Beyond the RPA, the elastic response is smeared out into a diffusive mode of non-zero width. This broadening may essentially eliminate the inelastic phason mode, leaving only a diffusive peak centred at zero energy in the long-wavelength limit. The intensity of this peak diverges, and its nominal width goes to zero, when the magnetic Bragg reflection is approached. However, a diffusive-like inelastic response is still present at $\mathbf{q} = \mathbf{0}$, and a true inelastic mode only appears some distance away. In the calculations, the elastic *single-site* response was assumed to be broadened by about 6 meV, corresponding to the spin-wave bandwidth. This assumption gives a reasonable account of the excitations in the long-wavelength limit, suggesting that they become overdamped if the wave-vector is less than about 0.1 times $2\pi/c$. Although the inelastic phason mode is largely eliminated, the calculations suggest that a residue may be observable. The most favourable conditions for detecting it would occur in a neutron-scattering scan with a large component of the scattering vector in the basal plane at about 50 K.

Another example to which the above theory has been applied is Tm (McEwen *et al.* 1991), where the c-axis moments order below 57.5 K in a longitudinally polarized structure, which becomes commensurable around 32 K. Below this temperature, as described in Section 2.3.1, the structure is ferrimagnetic, comprising four layers with the moments parallel to the c-axis, followed by three layers with the moments in the opposite direction. Although Tm belongs to the heavy end of the rare earth series, the scaling factor for the RKKY-exchange interaction, $(g-1)^2 = 1/36$, is small, and the Néel temperature is low compared to the crystal-field energy-splittings. The crystal-field effects are therefore more important in this element than in the other heavy rare earths. The energy difference between the MF ground state and the dipolar excited

state is calculated to vary between 8.0 and 10.2 meV, while the exchange field lies between 0 and 1.8 meV. Hence the exchange field acts as a minor perturbation, and incommensurable effects above 32 K in the excitation spectrum should be unimportant. In the low-temperature limit, the magnetic excitations are spin waves; the MF ground state and the first dipolar excited state are almost pure $|\pm 6>$ and $|\pm 5>$ levels (+ or $-$ depending on the site considered). The excitations propagating in the c-direction are found to lie between 8.5 and 10 meV (Fernandez-Baca *et al.* 1990; McEwen *et al.* 1991). The magnetic period is seven times that of the lattice, and the exchange coupling splits the spin waves into seven closely lying bands, which cannot be separated experimentally. With a finite resolution, the exchange coupling leads to a single or, at some wave-vectors, a double peak, whose shape and width change with **q**. At low temperatures, a relatively strong coupling between the spin waves and the transverse phonons is observed, and when this coupling is included in the determination of the RPA response functions, by the method presented in Section 7.3.1 in the next chapter, good agreement is obtained between the calculated neutron spectra and those observed experimentally. At elevated temperatures, both below and just above T_N, other excitations between the excited crystal-field (MF) levels are observed to be important, both in the transverse and the longitudinal components of the response function, and good agreement is again found between theory and experiment. With respect to its magnetic properties, Tm is thus an exceptional member of the heavy rare earths, as it is the only one in which well-defined crystal-field excitations have been detected. Hence it provides an appropriate termination of our discussion of spin-waves, as well as a natural transition to the crystal-field systems which are the topic of the next chapter.